Projection of land surface temperature considering the effects of future land change in the Taihu Lake Basin of China

Yongjiu Feng, Heping Li, Xioahua Tong, Lijuan Chen, Yang Liu

PII: S0921-8181(17)30490-3
DOI: doi:10.1016/j.gloplacha.2018.05.007
Reference: GLOBAL 2775

To appear in: *Global and Planetary Change*

Received date: 24 September 2017
Revised date: 19 May 2018
Accepted date: 20 May 2018

Please cite this article as: Yongjiu Feng, Heping Li, Xioahua Tong, Lijuan Chen, Yang Liu , Projection of land surface temperature considering the effects of future land change in the Taihu Lake Basin of China. The address for the corresponding author was captured as affiliation for all authors. Please check if appropriate. Global(2017), doi:10.1016/j.gloplacha.2018.05.007

Projection of land surface temperature considering the effects of future land change in the Taihu Lake Basin of China

Yongjiu Feng[1,2], Heping Li[1], Xioahua Tong[3*], Lijuan Chen[2,4], Yang Liu[1]

[1]College of Marine Sciences & National Distant-water Fisheries Engineering Research Center, Shanghai Ocean University, Shanghai 201306, China
[1]School of Earth and Environmental Sciences, The University of Queensland, Brisbane, 4072, Australia
[1]College of Surveying and Geo-Informatics, Tongji University, Shanghai 200092, China
[1]Key Laboratory of Ecohydrology of Inland River Basin, Northwest Institute of Eco-Environment and Resources, Chinese Academy of Sciences, Lanzhou, 730000, China

[*]Corresponding authors: Xiaohua Tong, Email: xhtong@tongji.edu.cn

Abstract:

Land surface temperature (LST) is an important environmental parameter that is significantly affected by land use and landscape composition. Despite the recent progress in LST retrieval algorithms and better knowledge of the relationship between LST and land coverage indices, predictive studies of future LST patterns are limited. Here, we project LST patterns in the Taihu Lake Basin to the year 2026 based on projected land use pattern and simulated land coverage indices that include normalized difference built-up index (NDBI), normalized difference vegetation index (NDVI) and normalized difference water index (NDWI). We derived the spatiotemporal LST patterns in the Taihu Lake Basin from 1996 to 2026 using thermal infrared data from Landsat imagery. A CA-Markov model was applied to project the 2026 land use pattern in the basin based on spatial driving factors, using the 2004 land use as the initial state. We simulated the NDBI, NDVI and NDWI indices for 2026 using the projected land use patterns, and then generated the 2026 LST in the study area. Our results showed that LST has been increasing and the warming areas have been expanding since 1996, especially in the Su-Xi-Chang urban agglomeration. The mean LST in Su-Xi-Chang has increased from less than 30°C in 1996 to greater than 31°C in 2004 and has risen to about 33°C in 2016, and the projection suggests that LST will reach about 35°C in 2026. Our results also suggest that mean LST increased by 2°C per decade in this highly urbanized area between 1996 and 2026. We present a preliminary method to produce future LST patterns and provide reasonable LST scenarios in the Taihu Lake Basin, which should help develop and implement management strategies for mitigating the effects of urban heat island.

Key words: land surface temperature (LST), land use change, future scenarios, CA-Markov, projection of LST; Taihu Lake Basin

1. Introduction

Land surface temperature (LST) is the radiative skin temperature of the land surface, which is significantly affected by factors including terrain condition, landscape composition, land coverage, urbanization and global change (Asgarian et al., 2015; Connors et al., 2013; Hamstead et al., 2016; Song et al., 2014). Urbanization and land use change are the most important anthropogenic influences on local climate (Chen et al., 2018; Garuma, 2017) that lead to urban heat island effects. The effects of land use on LST have been extensively studied over the past two decades (Amiri et al., 2009; Maimaitiyiming et al., 2014; Rahman et al., 2017; Weng et al., 2014), improving our understanding of the meteorological consequences of large-scale land use changes. However, few efforts have been made to evaluate the effects of future land use scenarios on LST or project future patterns of LST by considering potential land use changes. As a consequence, there is a need to develop new methods to project future LST distributions based on projections of future land use changes and land coverage indices.

LST is an important environmental parameter derived from ground measurements and thermal infrared (TIR) data from satellite sensors (Islam et al., 2017; Jiménez-Muñoz et al., 2014). Ground measurements cannot practically provide LSTs over large areas (Li et al., 2013) where the information can be derived from surface-outgoing radiance measurements from remote sensing (Jacob et al., 2017). The radiance measured by satellite radiometers depends on surface parameters and atmospheric effects (Guillevic et al., 2014). LST research has focused on the development of retrieval algorithms using TIR data from Landsat and Moderate Resolution Imaging Spectroradiometer (MODIS) and validation of LST-derived products. These algorithms can be categorized into two approaches: *known* and *unknown* land surface emissivity (LSE). Single-channel, multi-channel, and multi-angle are three widely applied LSE-*known* techniques. Stepwise retrieval of LST, and simultaneous retrieval of LSE and LST with known or unknown atmospheric information are two common LSE-*unknown* methods (Cristóbal et al., 2009; Gillespie et al., 2011; Li et al., 2013). These methods provide retrieval alternatives to obtain

relatively reliable LST information from TIR data, facilitating examination of land surface physical processes.

It has been recognized that land use change and landscape dynamics substantially influence the climate system (Mahmood et al., 2014). Therefore, investigation of the effects of land use on LST is particularly important because land use change is a local environmental issue with global consequences (Foley et al., 2005). There is strong interest in examining the relationships between land use and LST across space using remote sensing, geographical information systems (GIS) and statistical techniques. Urban heat islands have been extensively studied during the past two decades to explicitly address the human-induced, environmental and meteorological drivers of urban heating (Chen et al., 2006; Santamouris et al., 2015; Zhang et al., 2016). Relationships between urban heat island effects and land coverage indicators such as impervious surface area (ISA) and normalized difference vegetation index (NDVI) have been examined using remote sensing imagery and GIS (Li et al., 2011; Yuan and Bauer, 2007). Landscape patterns measured using landscape metrics (Feng et al., 2018) also significantly affect local climate via urban heat islands (Buyantuyev and Wu, 2010; Connors et al., 2013; Li et al., 2011). Moreover, LST is highly correlated with land coverage indices such as normalized difference built-up index (NDBI), normalized difference water index (NDWI) and NDVI (Zhang et al., 2009).

With our enhancing understanding of LST mechanism and the development of remote sensing technologies, researchers have paid much attention to the LST and urban heat island effects in mainland China during the past two decades (Guo et al., 2016; Li et al., 2011; Nie et al., 2016; Sheng et al., 2017). Chinese megacities such as Beijing, Shanghai, Guangzhou and Hangzhou are the case areas that have often been studied. For example, Li et al. (2012) studied how the spatial pattern of green space affects LST in Beijing, broadening our understanding of the relationship between LST and vegetation coverage. Nie et al. (2016) investigated how the ISA-LST relationship evolves with urbanization and how the spatiotemporal change in ISA

quantitatively affects LST in Shanghai. Guo et al. (2016) summarized the impact of urban morphology heterogeneity on LST in Guangzhou, suggesting that medium building height and a lower building density significantly cause higher LST. Sheng et al. (2017) conducted a comparative study of the urban heat island effects between air temperature and LST in Hangzhou. Regarding the urban heat island effects, their results suggest that LST performs best on hot sunny days while air temperature performs better during the nighttime following a dry day. Despite the progress of LST research in China, more efforts should be made to project future LST patterns to inform the public and local authorities, based on simulated future land use scenarios (Rahman et al., 2017; Tran et al., 2017).

New methods for LST projection from a spatial perspective are necessary and scientifically valuable. It is possible to assess the future LST pattern by establishing its relationships between land coverage indices including NDBI, NDVI and NDWI. Because these indices are closely associated with the land use patterns, we can project their future patterns if accurate projections of future land use are available. These scenarios can be simulated by cellular automata (CA), a widely applied dynamic geographical modeling framework.

This paper projects LST patterns in the Taihu Lake Basin out to the year 2026, based on predicted land use patterns and simulated NDBI, NDVI and NDWI indices. We derived the LST patterns from TIR data of Landsat images and analyzed their temporal changes in the Taihu Lake Basin in 1996, 2004 and 2016. A CA-Markov model embedded in Clark Labs' IDRISI® software (www.clarklabs.org) was applied to project the 2026 land use scenario based on spatial driving factors with the 2004 land use as the initial state. We then simulated NDBI, NDVI and NDWI indices for 2026 using the 2026 projected land use pattern. Finally, we generated the 2026 LST based on the relationships between the land coverage indices and LST in 2016, with the simulated 2026 land coverage indices as the input data.

The following section first briefly introduces the study area of the Taihu Lake Basin, then presents the spatial datasets used to derive and model LST. Section 3 describes the methodology applied in this paper, which includes land use classification, calculation of land coverage indices, LST derivation, CA-Markov modeling, and future LST projection. Section 4 presents the classified land use patterns and the observed land coverage indices, then examines the LST patterns from 1996 to 2016. The projected 2026 land use pattern and land coverage indices are presented in the same section 4, followed by the prediction of 2026 LST pattern and a discussion. Finally, the conclusions were drawn in Section 5.

2. Study area and datasets

2.1 Study area

Taihu Lake is the largest freshwater lake in the Yangtze River Delta of eastern China (Figure 1a-b) and is administered by Suzhou and Wuxi of Jiangsu Province. The Taihu Lake Basin comprises an annular region that incorporates five cities: Suzhou, Wuxi, Changzhou (the Su-Xi-Chang urban agglomeration) and Yixing in Jiangsu Province, and Huzhou in Zhejiang Province (Figure 1c). Yixing City is a satellite city of Wuxi and is individually listed here because it is isolated from the main part of Wuxi by Taihu Lake. The basin under study covers 27,513 km^2 and is a highly developed region with a 2015 total population of 17.5 million (Statistics Bureau of Jiangsu Province, 2016). Over the past two decades, the developed urban areas of the basin quadrupled from 547 km^2 in 1996 to 2,219 km^2 in 2016, while the rural settlement areas have increased from 3,253 km^2 to 4,145 km^2, as measured based on the land use patterns classified using Landsat imagery. Rapid urbanization accompanied by rapid industrialization has had negative effects on the environment, especially land cover and LST.

[Insert Figure 1 about here]

Figure 1 Location of Taihu Lake Basin and its administrative boundaries. (a) Yangtze River Delta, and (b) Taihu Lake Basin.

2.2 Raw data

Three Landsat images and a SRTM DEM v4 dataset were collected over the Taihu Lake Basin. The 1996 and 2004 Landsat images were from the Thematic Mapper (TM) while the 2016 image was from the Operational Land Imager (OLI). The images were acquired in the same season (26 July – 5 August) and were used to classify the land use patterns and derive LST. July and August are the hottest months of the year in the Taihu Lake Basin, and tend to have the highest LST. DEM was used to assist the classification and evaluate land development suitability. DEM reflects the topographical features of a region where the local organisms differ at different altitudes, implying soil type, temperature and humidity that are related to land cover. As such, DEM expands the attribute information of land cover to assist remote sensing classification. In the classification process, the elevation of a pixel is considered to adjust the land cover category defined by a classifier, hence improving the classification accuracy.

Moreover, the shape datasets such as topography and road networks were utilized to define the administrative boundary of each city and calculate the proximity to city centers, main roads, railways and existing built-up areas. These proximity variables are the main drivers of land use change that were embedded in CA-Markov to project future land use out to 2026.

[Insert Table 1 about here]

Table 1 Remote sensing images and vector dataset used in this paper

3. Methodology

3.1 Land use classification

The C5.0 decision tree classifier embedded in ENVI® 5.2 software (www.harris.com) was used to produce the land use patterns in 1996, 2004 and 2016. By integrating mathematical statistics and induction methods, a knowledge-based decision tree classifier considers the

spectral characteristics of ground objects and other spatial datasets (e.g. DEM) to construct classification rules, which are then used to classify remote sensing images. The C5.0 classification rules are easy to understand, and the classification process also conforms to the human cognitive process. The C5.0 is superior to a few supervised classifiers because the latter depends on regions of interest (a priori knowledge) and once these regions of interest are not properly selected, the classification results will not be sufficiently reasonable.

We first extracted brightness, greenness and wetness to interpret land use categories after radiation rectification and tasseled cap transformation (Figure 2). Brightness was used to discriminate between high and low-density built-up areas, while wetness and greenness were jointly applied to discriminate water bodies from forest (Wen et al., 2007). NDBI was utilized to discriminate low-density built-up areas from agricultural land. Landsat images from three periods in the Taihu Lake Basin were classified into five categories: high-density built-up areas, low-density built-up areas, agricultural lands, forests, and water bodies. The high-density built-up areas are highly impervious surfaces of urban areas, while the low-density built-up areas represent the rural residential lands. We collected the field survey (10% sampling) datasets of land use in 1996, 2004 and 2016 from local bureaus of planning and land resources, which were used to evaluate the land map categorization. The overall classification accuracies were 97.2% in 1996, 96.8% in 1996, and 96.3% in 2016, indicating the good performance of the C5.0 decision tree classifier.

[Insert Figure 2 about here]

Figure 2 Decision tree classifier for identifying land use pattern in the Taihu Lake Basin

3.2 Calculation and simulation of coverage indices

We calculated three land coverage indices: NDBI, NDVI and NDWI, all of which range between -1.0 and 1.0. NDBI is a widely used indicator for extracting the built-up areas (Varshney,

2013). NDVI is the most commonly applied vegetation index for monitoring vegetation condition and/or vegetation health (Eastman et al., 2013). NDWI is an indicator of open water features to enhance their presence in remote sensing images (Pettorelli, 2013). Using Landsat images, the three indices can mathematically be calculated by (Bouhennache et al., 2016; Rahman et al., 2017):

$$\begin{cases} \text{NDBI} = \dfrac{SWIR - NIR}{SWIR + NIR} = \dfrac{B5 - B4}{B5 + B4}(TM\&ETM^{+}) = \dfrac{B6 - B5}{B6 + B5}(OLI) & (1) \\ \text{NDVI} = \dfrac{NIR - Red}{NIR + Red} = \dfrac{B4 - B3}{B4 + B3}(TM\&ETM^{+}) = \dfrac{B5 - B4}{B5 + B4}(OLI) & (2) \\ \text{NDWI} = \dfrac{GREEN - NIR}{GREEN - NIR} = \dfrac{B2 - B4}{B2 + B4}(TM\&ETM^{+}) = \dfrac{B3 - B5}{B3 + B5}(OLI) & (3) \end{cases}$$

where NIR represents the near-infrared spectrum, SWIR represents the short-wavelength infrared spectrum, RED represents the red spectrum, and GREEN represents the green spectrum.

To simulate future coverage indices, we used a method that reflects both structural and local variations of these indices. The simulation workflow is illustrated in Figure 3 using NDVI as an example. The structural component indicates the global change of the coverage indices over time, while the local component indicates the local index variations caused by land use change. After an integrated analysis of NDVI change during the past two decades from 1996–2016, we modeled the 2026 NDVI as an input layer for future LST projection. The NDBI and NDWI indices for the year 2026 were calculated using a similar method.

[Insert Figure 3 about here]

Figure 3 The method to simulate future coverage indices with an example of NDVI

3.3 LST Derivation

LST is derived using a complicated procedure related to land coverage, surface emissivity, atmospheric radiation correction, and radiation transmission. LST can be derived from Landsat-5 TM and Landsat-8 OLI images by the following steps:

- **Calculation of vegetation coverage** The NDVI maps are the basic data used to derive the surface vegetation coverage and deduce the land surface emissivity of various land use categories. The NDVI calculation is given by Equation (2) for TM and OLI images. Based on the calculated NDVI, the vegetation coverage can then be given by:

$$Pv = \frac{NDVI - NDVI_{\text{soil}}}{NDVI_{\text{vegetation}} - NDVI_{\text{soil}}} \tag{4}$$

where NDVI denotes the original value of NDVI, $NDVI_{soil}$ (0.0) denotes the NDVI value of bare soil areas or areas with absolutely no vegetation coverage, and $NDVI_{vegetation}$ (0.7) denotes the NDVI value of areas completely covered by vegetation.

- **Calculation of land surface emissivity** The spectral emissivity is the ratio between the radiance emitted by a natural object and that emitted by a blackbody at the same temperature. We followed (Sobrino et al., 2004) and (Jiménez-Muñoz et al., 2014) to define the spectral emissivity of various land surfaces given by:

$$\begin{cases} \varepsilon_w = 0.995 & (5) \\ \varepsilon_n = 0.9625 + 0.0614Pv - 0.0461Pv^2 & (6) \\ \varepsilon_b = 0.9589 + 0.086Pv - 0.0671Pv^2 & (7) \end{cases}$$

where ε_w denotes the spectral emissivity of water bodies, ε_n denotes the spectral emissivity of natural surfaces, and ε_b denotes the spectral emissivity of built-up areas.

- **Atmospheric radiation correction** The thermal infrared radiation received by satellite sensors is complex and is composed of [1] the upwelling radiance (L↑) of the atmosphere, [2] the radiation (ε) that goes out from the surface through the atmosphere and ultimately reaches satellite sensors, and [3] the reflected downwelling irradiance (L↓) from the atmosphere. Therefore, the thermal infrared radiation [L(λ)] is given by:

$$L(\lambda) = (\varepsilon \cdot B(TS) + (1 - \varepsilon) \cdot L\downarrow) \cdot \tau + L\uparrow \tag{8}$$

where ε is the land surface emissivity, TS is the real temperature of land surface, $B(TS)$ is the thermal radiation of the blackbody at the TS temperature according to Planck's law, τ is the transmittance of the atmosphere within the infrared band. As a result, the thermal radiation $B(TS)$ of the blackbody at the TS temperature is calculated as:

$$B(TS) = (L(\lambda) - L\uparrow - \tau \cdot (1-\varepsilon) \cdot L\downarrow)/\tau \cdot \varepsilon \quad (9)$$

where the parameters at the central point of the images (31.75°N, 120.30°E) are used in the calculation. For 5 August 1996, τ was 0.6, $L\uparrow$ was 3.39 W/(m^2·sr·μm), and $L\downarrow$ was 5.12 W/(m^2·sr·μm); for 26 July 2004, τ was 0.54, $L\uparrow$ was 3.97 W/(m^2·sr·μm), and $L\downarrow$ was 5.84 W/(m^2·sr·μm); for 27 July 2016, τ was 0.43, $L\uparrow$ was 5.15 W/(m^2·sr·μm), and $L\downarrow$ was 7.39 W/(m^2·sr·μm).

- **Calculation of LST** After retrieving the thermal radiation $B(TS)$ of the blackbody, the LST can be calculated using an inverse Planck law:

$$LST = \frac{K2}{\ln(K1/B(TS)+1)} - 273 \quad (10)$$

where K1=666.09W/(m^2·sr·μm) and K2=1282.71K for TM/ETM+ images while K1=774.89W/(m^2·sr·μm) and K2=1321.08K for OLI images, with the LST expressed in °C.

3.4 Modeling future land use using CA-Markov

CA is a bottom-to-top modeling framework (Feng et al., 2016; Feng and Tong, 2018) whose ability to predict future land use is strengthened by integration with Markov model (Mitsova et al., 2011; Sang et al., 2011). The CA-Markov model is available in IDRISI® and is readily applicable to simulate multiple land use changes and project the future scenarios. In this hybrid model, Markov is used for calculation of the land transition area, a statistical method (*e.g.* logistic regression) is used to assess land transition suitability, and CA is used to allocate land cells. The three main components in the CA-Markov workflow are:

- **Markov transition estimation** The Markov estimates transition probabilities, transition areas, and conditional probability images by comparing two land cover images. The transition probability matrix denotes the likelihood that one land use category will change state to another. The transition areas matrix identifies cells that are expected to change from one land use category to another during a specific time period. The conditional probability images provide the quantity of expected land use change from each existing category to

every other category in the next time period.

- **Land transition suitability** The suitability maps are commonly generated using logistic regression and are based on the relationships between land use changes and their drivers. Each transition suitability map corresponds to a land use category produced using logistic regression modeling by DIRISI or by using statistical software modules and the Spatial Analyst tool in ArcGIS.
- **CA modeling** The neighborhood effect represents local interactions among different land use categories. An extended Moore neighborhood configuration that contains 5×5 neighboring cells was used in this work. Moreover, the number of CA iterations is defined before implementation, where an iteration represents one year.

3.5 Projection of future LST

Land coverage indices including NDBI, NDVI and NDWI have a robust relationship with LST (Sun et al., 2012; Zhang et al., 2009). We therefore examined the relationships between the LST and the three indices for 2016 by exhaustive testing of all possible combinations (including interaction). Among the combinations, this expression exhibits the best goodness-of-fit R^2 (0.6875):

$$\mathrm{LST} = 33.48 + 8.66\mathrm{NDBI} + 2.9\mathrm{NDVI} - 4.01\mathrm{NDWI} + 13.34\mathrm{NDBI} \times \mathrm{NDVI} \quad (11)$$

Equation (11) was used to project future LST to the year 2026 using the three simulated land coverage indices in 2026.

4. Results and discussion

4.1 Land use patterns and land coverage indices

The major change in land use and cover in the Taihu Lake Basin was linked to a significant increase in high and low-density built-up areas, sacrificing valuable agricultural land (Figure 4 and Table 2). The urban extent (the high-density built-up area) of Su-Xi-Chang expanded by a

vast area of 3,466 km^2 during the last decade, mainly due to the population increase, economic prosperity and booming housing market. The 1,871 km^2 increase in rural settlement area (*i.e.* the low-density built-up area) is small, compared to the urban increase. We note that the urbanization rate in the Taihu Lake Basin has grown from below 30% in 1996 to nearly 50% in 2016 (Table 2). In contrast, the forested areas and water bodies experienced much less change as compared with built-up areas and agricultural lands.

[Insert Figure 4 about here]

Figure 4 Land use and land cover change in the Taihu Lake Basin during 1996 to 2016. (a) 1996 land pattern, (b) 2004 land pattern, and (c) 2016 land pattern.

[Insert Table 2 about here]

Table 2 Land use change in area and percentage in the Taihu Lake Basin during 1996 to 2016

To project land coverage indices for 2026, we derived land coverage indices in 2016 (Figure 5) and identified their relationships with respect to LST (Equation 11). Except for water bodies, the NDBI and MDVI indices appear to be negatively correlated, but both indicate similar land use patterns (Figures 5a-b). Specifically, the Su-Xi-Chang areas show relatively high built-up density but low vegetation coverage, while the other regions (especially Huzhou) show relatively low built-up density and high vegetation coverage. The NDWI of water bodies is the highest, followed by moderate values in low-lying areas and the lowest values in high-slope areas (Figure 5c).

[Insert Figure 5 about here]

Figure 5 Land coverage demonstrated by NDBI, NDVI and NDWI for 2016 in the Taihu Lake Basin. (a) 2016 NDBI, (b) 2016 NDVI, and (c) 2016 NDWI.

4.2 Spatiotemporal patterns of LST

The spatial patterns show clearly that the high LST areas are mainly observed in the Su-Xi-Chang urban agglomeration, and have been expanding since 1996 (Figure 6). The highest LST continuously increased from 49.8°C in 1996 to 54.9°C in 2016, while the lowest LST showed a fluctuation during 1996-2016, with a higher value occurring in 2004. Among all land use categories, the built-up areas have the highest LST, followed by agricultural land, forest and water bodies, in descending order (Table 3). The mean LST in agricultural lands displayed the largest increase from 1996 to 2016 (4.4°C), while the mean LST increase in forest areas had the smallest increase (2.2°C), reflecting the effects of land use and cover change. In the spatial domain, Wuxi had the highest mean LST (29.6°C) in 1996, Wuxi and Suzhou had similar high mean LST (~ 31°C) in 2004, and the three cities in the Su-Xi-Chang urban agglomeration had similar high mean LSTs (above 33°C) in 2016.

[Insert Figure 6 about here]

Figure 6 Spatial patterns of LST in the Taihu Lake Basin from 1996 to 2016. (a) 1996 LST, (b) 2004 LST, and (c) 2016 LST.

[Insert Table 3 about here]

Table 3 Summary statistics of LST in relation to land use categories and administrative regions

The area and percentage of high LST continued to increase from 1996 to 2016 based on the groupings with an interval of 5°C (Table 4). In 1996, LSTs between 25° and 35°C occupied 85.3% of the study area, while only a few areas had LSTs below 20°C or above 40°C. In 2004, the dominant LST range (25°C-35°C) decreased to 77.2%, mainly attributed to the areal increases of both the lower (20°C-25°C) and higher (35°C-40°C) LST ranges. However, the LST areas and percentages less than 20°C are zero, while only a few land cells had the LST higher than 40°C. The 2016 LSTs were generally higher than in 1996 and 2004, which had a wider dominant LST range (25°C-40°C) covering 97.7% of the total area. Only a few land cells had LSTs between

45°C and 50°C, and those with LST higher than 50°C are effectively zero.

[Insert Table 4 about here]

Table 4 Summary statistics of LSTs based on their ranges in relation to area and percentage

4.3 Simulating land use pattern and coverage indices to the year 2026

Land use patterns for the year 2026 (Figure 7a) were simulated using the calibrated CA-Markov model. Significant land use changes are forecast during 2016–2026, with major increases in high and low-density built-up areas and a noticeable decrease in agricultural lands (Figure 7b). Specifically, the high-density built-up areas will gain 1,857 km^2 (6.8% of the study area) and the low-density built-up areas will gain 1,046 km^2 (3.8%), whereas the agricultural land will lose 2,990 km^2 (10.9%). Meanwhile, forested areas and water bodies will change by only about 1%. Such a dramatic land use change will lead to an increase in the total impervious surface area and major changes in the environment over the next ten years, leading to a continued general increase in LST.

Based on the projected 2026 land use pattern, we modeled three land coverage indices (Figures 7c-e) using the workflow of Figure 3. The three 2026 coverage pattern indices are quite similar to the 2016 patterns, but visual inspection identifies smaller differences between sub-regions for all three 2016 indices when compared with those from 2016, suggesting reduced deviance for all indices. Specifically, NDBI increases slightly while NDVI decreases significantly, except in water bodies. NDWI decreases slightly for water bodies but increases slightly for all other land use categories. These drastic changes in land use and land coverage indicate that there will be a great change in LST for 2026.

[Insert Figure 7 about here]

Figure 7 The simulated land use pattern and land coverage indices for the year 2026. (a)

Projected land use pattern of 2026, (b) Land use change between 2016-2026, (c) 2026 NDBI, (d) 2026 NDVI, and (e) 2026 NDWI.

4.4 Projecting 2026 LST

The projected 2026 LST (Figure 8a) was calculated using Equation (11) with three simulated land coverage indices as input layers. The result shows a significant LST increase during the 2016–2026 decade. The summary statistics presented in Table 5 show that the mean LSTs of high and low-density built-up areas are very high (40.7°C and 36.8°C, respectively), followed by those of agricultural land and forest (about 34°C) and that of water bodies (below 30°C). The LST in the Su-Xi-Chang urban agglomeration will be higher than in other regions including Yixing, Huzhou and the Taihu Lake. Of all regions, Wuxi will have the highest LST in 2026. The dominant LST range is 25°C–45°C and the areas with LST between 35°C–40°C represent approximately half of the study area with a significant increase in LST. The areas with LST lower than 25°C or higher than 45°C are very small. Compared with 2016, the mean LST in 2026 will increase by about 6°C in high-density built-up areas, while it will increase by about 3°C in low-density built-up area (Tables 4 and 5). LST in forested areas will be close to that of agricultural lands, while the LST of water bodies will increase by only about 1°C. In summary, land use change will have a greater effect on the temperature of land surfaces than on water bodies.

Compared with the 2016 LSTs, 2026 LSTs below 25°C will effectively disappear. The highest LST areas will not change markedly (Tables 4 and 5). From 2016 to 2026, 89.4% of the study area will become significantly warmer while only 10.6% will become slightly cooler. Approximately 55% of the study area will see an LST increase of 0–5°C while about 31% of the study area will see a 5–10°C LST increase (Figure 8b), reflecting significant changes in land surfaces from 2016 to 2026.

[Insert Figure 8 about here]

Figure 8 The projected LST for 2026 and its change between 2016–2026 in the Taihu Lake Basin. (a) Projected LST for the year 2026, and (b) Difference map of LST between 2016-2026.

[Insert Table 5 about here]

Table 5 Summary statistics of LSTs in 2026 and their ranges in relation to area and percentage

4.5 Discussion

Based on the assumption that land coverage is closely linked with LST, we can project future LST patterns using an accurate projection of future land use. The Markov chain integrated CA model is a robust modeling framework that is based on the relationships between land use change and its drivers, and on the land transition probabilities between multiple land use categories. It has been shown that CA-Markov can well simulate future land use scenarios (the overall accuracy is about 85%) and explore the possible patterns of land use in the future (Arsanjani et al., 2013; Moghadam and Helbich, 2013). As such, future LST projection depends principally on an accurate projection of the indicators. Our method of projecting land coverage indices is similar to the Kriging approach to interpolation of geostatistics, which decomposes the temporal change of indices into structural and local components. Using this method, we generated reasonable land coverage indices NDBI, NDVI and NDWI and used them to project LST to the year 2026.

Our results show that the past and future rises of LST in the basin are remarkable. Although the increases might be influenced by many factors, the rapid urbanization, industrialization, and human activities caused by highly concentrated population should probably be considered as the dominant factors. The urban growth rate (from 28.9% in 1996 to 48.3% in 2016) in the basin is comparable to many other rapidly urbanizing areas of China such as Beijing, Shanghai, Hangzhou and Guangzhou (Li et al., 2011). For example, the built-up area in Beijing expanded

from 18% in 2001 to 32% in 2010 while the urbanized area in Shanghai grown from 18% in 2005 to 38% in 2015 (Feng and Tong, 2017; Li et al., 2012); the built-up area in Hangzhou increased from 17% in 2005 to 27% in 2015 while the urbanized area in Guangzhou raised from 14% in 2003 to 36% in 2010 (Sheng et al., 2017; Sun et al., 2012). In these regions, the negative impacts of urbanization may outweigh the benefits, which can be manifested by the increasing LST and ecological degradation. Previous studies have shown that the impervious surface area (built-up area) is an accurate indicator of urban heat island effects, defined by a strong linear relationship with LST (Mathew et al., 2016; Zhang et al., 2009). In economically developed regions such as Su-Xi-Chang in the basin, our research shows that the impervious surface areas have continuously expanded due to large-scale urban construction, a vigorous housing market, and strong demand for industrial land, resulting in changes in the land surface environment, and hence increasing LST.

In the Su-Xi-Chang urban agglomeration of the basin, LST has been increasing and the warming areas have been expanding since 1996. Mean LST in Su-Xi-Chang increased from less than 30°C in 1996 to greater than 31°C by 2004, and increased further to 33°C by 2016. Our projection suggests that mean LST in Su-Xi-Chang will reach about 35°C in 2026. This result suggests the mean LST increases of 2°C per decade over the highly urbanized area, with LST increasing by about 5°C–10°C in few sub-regions. Areas covered by vegetation and water bodies show lower increases in LST than urbanized areas. By 2026, about 18% of our study area is envisaged to have mean LST over 40°C, lower than those in Dammam of Saudi Arabia and Hanoi of Vietnam (Rahman et al., 2017; Tran et al., 2017). A projection of future LST in Dammam shows that, by 2026, the urban area is expected to encompass 55% of the city and 98% of the land cover is envisioned to have mean LST over 41°C (Rahman et al., 2017). The LST prediction in Hanoi inner city shows that, by 2023, 56% of Hanoi area is envisaged to have mean LST above 40.5°C (Tran et al., 2017). This may be because Dammam has a desert climate with low vegetation coverage (~5%) while Hanoi has a warm, humid subtropical climate with hot

summers. In contrast, our study area has a typical subtropical monsoon climate with high vegetation coverage (~28%) and high freshwater coverage (~23%).

The LST derivation from remote sensing and the projection by modeling should be able to alert us the future LST scenario, and have important implications for land use management to mitigate the urban heat islands. The Taihu Lake Basin is an important area in eastern China, not only because of its geographical advantages in transportation and its natural environment, but also because of the proximal location of three highly developed prefecture-level cities (the Su-Xi-Chang urban agglomeration). From a macroscopic perspective, the factors that drive LST change can be roughly expressed as a top-to-bottom process beginning with management strategies to urban expansion and vegetation cover reduction, producing LST increases with concomitant urban heat island effects. Our research suggests that implementing management strategies to control the urban built-up extent is a solution for mitigating urban heat island effects. Construction and optimization of urban green spaces should also be a feasible solution to reduce the effects of heat islands, hence improving the environmental quality and enhancing the self-adjusting ability of urban ecological systems.

5. Conclusions

We have examined the spatiotemporal dynamics of LST in relation to land use change in the Taihu Lake Basin using Landsat imagery. We show that LST in the study area has been increasing since 1996 in response to major changes in land use. The high-density built-up areas are the warmest land surfaces, followed in decreasing order by low-density built-up areas, agricultural lands, forests, and water bodies. Apart from a better understanding of LST in the basin, we confirmed complex relationships between LST and the land coverage indices NDBI, NDVI and NDWI using interactive linear modeling. Two important outcomes of our work are [1] simulation of future land coverage indices based on projected future land cover, and [2] projection of future LST signaling the effect of land use change on a key land surface parameter.

Limitations of our work should be noted. First, the ground temperature measurements have not been validated and the summary statistics of LST for each land use category may be affected by land use classification. Second, the projection of LST for 2026 was realized using an empirical function built from the relationships between LST and land coverage indices only in 2016, which may compromise the accuracy of LST. As a consequence, the deviance of the projected LST for 2026 is smaller than those of the LSTs derived from Landsat images in earlier years. We will further analyze these limitations in future studies.

Our research presents a method to predict future LST patterns using remote sensing and GIS, and provides plausible scenarios for both land use and LST in the Taihu Lake Basin that are useful in developing regulations and management strategies to migrate urban heat island effects, thereby contributing to more sustainable and environmentally healthy cities.

Acknowledgment

We would like to thank Editor Liviu Matenco and two anonymous reviewers for providing constructive comments and helpful feedback on the original manuscript. This study was supported by the National Natural Science Foundation of China (41771414).

References

Amiri, R., Weng, Q., Alimohammadi, A. and Alavipanah, S.K., 2009. Spatial–temporal dynamics of land surface temperature in relation to fractional vegetation cover and land use/cover in the Tabriz urban area, Iran. Remote sensing of environment, 113(12), 2606-2617.

Arsanjani, J.J., Helbich, M., Kainz, W. and Boloorani, A.D., 2013. Integration of logistic regression, Markov chain and cellular automata models to simulate urban expansion. International Journal of Applied Earth Observation and Geoinformation, 21, 265-275.

Asgarian, A., Amiri, B.J. and Sakieh, Y., 2015. Assessing the effect of green cover spatial patterns on urban land surface temperature using landscape metrics approach. Urban Ecosystems, 18(1), 209-222.

Bouhennache, R., Bouden, T., Taleb, A. and Chaddad, A., 2016. Extraction of urban land features from TM Landsat image using the land features index and Tasseled cap transformation. Extraction, 1, 33037.

Buyantuyev, A. and Wu, J., 2010. Urban heat islands and landscape heterogeneity: linking spatiotemporal variations in surface temperatures to land-cover and socioeconomic patterns. Landscape ecology, 25(1), 17-33.

Chen, R., Zhang, Y., Xu, D. and Liu, M., 2018. Climate Change and Coastal Megacities: Disaster Risk Assessment and Responses in Shanghai City. In: S. Mal, R.B. Singh and C. Huggel (Eds.), Climate Change, Extreme Events and Disaster Risk Reduction: Towards Sustainable Development Goals. Springer International Publishing, Cham, pp. 203-216.

Chen, X.-L., Zhao, H.-M., Li, P.-X. and Yin, Z.-Y., 2006. Remote sensing image-based analysis of the relationship between urban heat island and land use/cover changes. Remote sensing of environment, 104(2), 133-146.

Connors, J.P., Galletti, C.S. and Chow, W.T., 2013. Landscape configuration and urban heat island effects: assessing the relationship between landscape characteristics and land surface temperature in Phoenix, Arizona. Landscape ecology, 28(2), 271-283.

Cristóbal, J., Jiménez‐Muñoz, J., Sobrino, J., Ninyerola, M. and Pons, X., 2009. Improvements in land surface temperature retrieval from the Landsat series thermal band using water vapor and air temperature. Journal of Geophysical Research: Atmospheres, 114(D8).

Eastman, J., Sangermano, F., Machado, E., Rogan, J. and Anyamba, A., 2013. Global Trends in Seasonality of Normalized Difference Vegetation Index (NDVI), 1982–2011. Remote Sensing, 5(10), 4799.

Feng, Y., Liu, M., Chen, L. and Liu, Y., 2016. Simulation of dynamic urban growth with partial least squares regression-based cellular automata in a GIS environment. ISPRS International Journal of Geo-Information, 5(12), 243.

Feng, Y., Liu, Y. and Tong, X., 2018. Spatiotemporal variation of landscape patterns and their spatial determinants in Shanghai, China. Ecological Indicators, 87, 22-32.

Feng, Y. and Tong, X., 2017. Calibrating nonparametric cellular automata with a generalized additive model to simulate dynamic urban growth. Environmental Earth Sciences, 76(14), 496.

Feng, Y. and Tong, X., 2018. Calibration of cellular automata models using differential evolution to simulate present and future land use. Transactions in GIS, https://doi.org/10.1111/tgis.12331.

Foley, J.A. et al., 2005. Global consequences of land use. science, 309(5734), 570-574.

Garuma, G.F., 2017. Review of urban surface parameterizations for numerical climate models. Urban Climate.

Gillespie, A.R. et al., 2011. Residual errors in ASTER temperature and emissivity standard products AST08 and AST05. Remote Sensing of Environment, 115(12), 3681-3694.

Guillevic, P.C. et al., 2014. Validation of Land Surface Temperature products derived from the Visible Infrared

Imaging Radiometer Suite (VIIRS) using ground-based and heritage satellite measurements. Remote Sensing of Environment, 154(Supplement C), 19-37.

Guo, G., Zhou, X., Wu, Z., Xiao, R. and Chen, Y., 2016. Characterizing the impact of urban morphology heterogeneity on land surface temperature in Guangzhou, China. Environmental Modelling & Software, 84(Supplement C), 427-439.

Hamstead, Z.A., Kremer, P., Larondelle, N., McPhearson, T. and Haase, D., 2016. Classification of the heterogeneous structure of urban landscapes (STURLA) as an indicator of landscape function applied to surface temperature in New York City. Ecological Indicators, 70(Supplement C), 574-585.

Islam, T. et al., 2017. A Physics-Based Algorithm for the Simultaneous Retrieval of Land Surface Temperature and Emissivity From VIIRS Thermal Infrared Data. IEEE Transactions on Geoscience and Remote Sensing, 55(1), 563-576.

Jacob, F. et al., 2017. Reassessment of the temperature-emissivity separation from multispectral thermal infrared data: Introducing the impact of vegetation canopy by simulating the cavity effect with the SAIL-Thermique model. Remote Sensing of Environment, 198(Supplement C), 160-172.

Jiménez-Muñoz, J.C., Sobrino, J.A., Skoković, D., Mattar, C. and Cristóbal, J., 2014. Land surface temperature retrieval methods from Landsat-8 thermal infrared sensor data. IEEE Geoscience and Remote Sensing Letters, 11(10), 1840-1843.

Li, J. et al., 2011. Impacts of landscape structure on surface urban heat islands: a case study of Shanghai, China. Remote Sensing of Environment, 115(12), 3249-3263.

Li, X., Zhou, W., Ouyang, Z., Xu, W. and Zheng, H., 2012. Spatial pattern of greenspace affects land surface temperature: evidence from the heavily urbanized Beijing metropolitan area, China. Landscape Ecology, 27(6), 887-898.

Li, Z.-L. et al., 2013. Satellite-derived land surface temperature: Current status and perspectives. Remote Sensing of Environment, 131, 14-37.

Mahmood, R. et al., 2014. Land cover changes and their biogeophysical effects on climate. International Journal of Climatology, 34(4), 929-953.

Maimaitiyiming, M. et al., 2014. Effects of green space spatial pattern on land surface temperature: Implications for sustainable urban planning and climate change adaptation. ISPRS Journal of Photogrammetry and Remote Sensing, 89(Supplement C), 59-66.

Mathew, A., Khandelwal, S. and Kaul, N., 2016. Spatial and temporal variations of urban heat island effect and the effect of percentage impervious surface area and elevation on land surface temperature: Study of Chandigarh city, India. Sustainable Cities and Society, 26(Supplement C), 264-277.

Mitsova, D., Shuster, W. and Wang, X., 2011. A cellular automata model of land cover change to integrate urban growth with open space conservation. Landscape and Urban Planning, 99(2), 141-153.

Moghadam, H.S. and Helbich, M., 2013. Spatiotemporal urbanization processes in the megacity of Mumbai, India: a Markov chains-cellular automata urban growth model. Applied Geography, 40, 140-149.

Nie, Q., Man, W., Li, Z. and Huang, Y., 2016. Spatiotemporal Impact of Urban Impervious Surface on Land Surface Temperature in Shanghai, China. Canadian Journal of Remote Sensing, 42(6), 680-689.

Pettorelli, N., 2013. The normalized difference vegetation index. Oxford University Press.

Rahman, M.T., Aldosary, A.S. and Mortoja, M.G., 2017. Modeling Future Land Cover Changes and Their Effects on the Land Surface Temperatures in the Saudi Arabian Eastern Coastal City of Dammam. Land, 6(2), 36.

Sang, L., Zhang, C., Yang, J., Zhu, D. and Yun, W., 2011. Simulation of land use spatial pattern of towns and villages based on CA–Markov model. Mathematical and Computer Modelling, 54(3), 938-943.

Santamouris, M., Cartalis, C., Synnefa, A. and Kolokotsa, D., 2015. On the impact of urban heat island and global warming on the power demand and electricity consumption of buildings—A review. Energy and Buildings, 98(Supplement C), 119-124.

Sheng, L., Tang, X., You, H., Gu, Q. and Hu, H., 2017. Comparison of the urban heat island intensity quantified by using air temperature and Landsat land surface temperature in Hangzhou, China. Ecological Indicators, 72(Supplement C), 738-746.

Sobrino, J.A., Jiménez-Muñoz, J.C. and Paolini, L., 2004. Land surface temperature retrieval from LANDSAT TM 5. Remote Sensing of environment, 90(4), 434-440.

Song, J., Du, S., Feng, X. and Guo, L., 2014. The relationships between landscape compositions and land surface temperature: Quantifying their resolution sensitivity with spatial regression models. Landscape and Urban Planning, 123(Supplement C), 145-157.

Statistics Bureau of Jiangsu Province, 2016. Jiangsu Statistical Yearbook of 2015. Beijing: China Statistics Press.

Sun, Q., Wu, Z. and Tan, J., 2012. The relationship between land surface temperature and land use/land cover in Guangzhou, China. Environmental Earth Sciences, 65(6), 1687-1694.

Tran, D.X. et al., 2017. Characterizing the relationship between land use land cover change and land surface temperature. ISPRS Journal of Photogrammetry and Remote Sensing, 124(Supplement C), 119-132.

Varshney, A., 2013. Improved NDBI differencing algorithm for built-up regions change detection from remote-sensing data: an automated approach. Remote Sensing Letters, 4(5), 504-512.

Wen, X., Hu, G. and Yang, X., 2007. Extracting Information from ETM+ Image Using C5 .0 Decision Tree Algorithm. Geography and Geo-Information Science, 23(6), 26-29.

Weng, Q., Fu, P. and Gao, F., 2014. Generating daily land surface temperature at Landsat resolution by fusing Landsat and MODIS data. Remote Sensing of Environment, 145(Supplement C), 55-67.

Yuan, F. and Bauer, M.E., 2007. Comparison of impervious surface area and normalized difference vegetation index as indicators of surface urban heat island effects in Landsat imagery. Remote sensing of Environment, 106(3), 375-386.

Zhang, N., Wang, X., Chen, Y., Dai, W. and Wang, X., 2016. Numerical simulations on influence of urban land cover expansion and anthropogenic heat release on urban meteorological environment in Pearl River Delta. Theoretical and Applied Climatology, 126(3), 469-479.

Zhang, Y., Odeh, I.O. and Han, C., 2009. Bi-temporal characterization of land surface temperature in relation to impervious surface area, NDVI and NDBI, using a sub-pixel image analysis. International Journal of Applied Earth Observation and Geoinformation, 11(4), 256-264.

List of Tables

Table 1 Remote sensing images and vector dataset used in this paper

Table 2 Land use change in area and percentage in the Taihu Lake Basin during 1996 to 2016

Table 3 Summary statistics of LST in relation to land use categories and administrative regions

Table 4 Summary statistics of LSTs based on their ranges in relation to area and percentage

Table 5 Summary statistics of LSTs in 2026 and their ranges in relation to area and percentage

Table 1 Remote sensing images and vector dataset used in this paper

Type	Source	Date	Spatial resolution	Operation	Purpose
Remote sensing	Landsat-5 TM	1996-08-05	30 m	Classify land use categories and derive LST	Mapping LST and projecting future land use
	Landsat-5 TM	2004-07-26	30 m	Classify land use categories and derive LST	
	Landsat-8 OLI	2016-07-27	30 m	Classify land use categories, extract shorelines and derive LST	
	SRTM DEM v4	2008-11-25	90 m	Calculate land slope	
Vector dataset	Topographic map	2015	1:5000	Define boundaries, city and county centers	Projecting future land use
	Road networks	2015	1:5000	Derive main roads and railways	

Table 2 Land use change in area and percentage in the Taihu Lake Basin during 1996 to 2016

Land use category	1996		2004		2015	
	Area (km^2)	*Percent*	*Area* (km^2)	*Percent*	*Area* (km^2)	*Percent*
High-density built-up area	1,156	4.2	3,081	11.2	4,622	16.8
Low-density built-up area	6,796	24.7	8,502	30.9	8,667	31.5
Agricultural land	10,895	39.6	6,768	24.6	5,750	20.9
Forest	2,641	9.6	2,916	10.6	2,036	7.4
Water body	6,025	21.9	6,273	22.8	6,438	23.4
Total	27,513	100	27,513	100	27,513	100

Table 3 Summary statistics of LST in relation to land use categories and administrative regions

Land use and administrative region		1996 (°C)			2004 (°C)			2016 (°C)		
		Min	Mean	Max	Min	Mean	Max	Min	Mean	Max
Land use	High-density built-up area	24.3	31.4	49.8	25.0	32.3	53.3	25.1	34.8	54.9
	Low-density built-up area	21.3	30.2	48.8	22.2	31.0	50.3	22.3	33.6	52.1
	Agricultural land	23.8	28.3	38.8	25.1	28.8	49.1	25.1	32.7	49.8
	Forest	20.0	26.2	37.5	21.3	27.6	39.5	21.0	28.4	44.9
	Water body	18.2	24.3	36.8	20.0	25.1	39.2	19.0	28.0	43.5
Administrative Region	Taihu Lake	20.1	24.0	36.8	22.0	24.9	40.9	19.0	28.1	49.4
	Yixing	20.0	28.7	41.7	21.3	29.9	45.8	19.2	31.8	54.5
	Changzhou	18.2	28.1	43.7	20.3	29.3	45.9	19.2	33.3	48.3
	Wuxi	20.8	29.6	42.5	22.3	30.9	45.4	19.1	33.3	54.9
	Suzhou	20.3	28.3	43.6	20.1	30.7	53.3	19.1	33.9	54.5
	Huzhou	20.2	28.9	49.8	20.0	28.6	47.7	19.0	31.7	51.3

Table 4 Summary statistics of LSTs based on their ranges in relation to area and percentage

LST range (°C)	1996		2004		2016	
	Area (km^2)	Percent	Area (km^2)	Percent	Area (km^2)	Percent
<20	~0	~0.0	0	0.0	~0	~0
20 to 25	3,604	13.1	4,952	18.0	275	1.0
25 to 30	17,718	64.5	11,941	43.4	8,969	32.6
30 to 35	5,750	20.9	9,299	33.8	13,069	47.5
35 to 40	413	1.5	1,266	4.6	4,842	17.6
40 to 45	~0.0	~0.0	83	0.2	275	1.0
45 to 50	~0.0	~0.0	~0.0	~0.0	83	0.3
>50	0	0	~0.0	~0.0	~0.0	~0.0
Total	27,513	100.0	27,513	100.0	27,513	100.0

Table 5 Summary statistics of LSTs in 2026 and their ranges in relation to area and percentage

Land use and administrative region	Min (°C)	Mean (°C)	Max (°C)		LST range (°C)	Area (km^2)	Percent
High-density built-up area	25.0	40.7	55.0		<20	0	0.0
Low-density built-up area	22.4	36.8	53.5		20 to 25	1	~0
Agricultural land	26.9	34.7	50.9		25 to 30	6083	22.1
Forest	22.5	34.0	48.9		30 to 35	3982	14.5
Water body	20.0	29.2	47.9		35 to 40	12544	45.6
Taihu lake	23.7	29.5	48.8		40 to 45	4899	17.8
Yixing	22.1	36.5	49.7		45 to 50	5	0.0*
Changzhou	21.9	37.2	52.6		>50	~0	~0
Wuxi	23.0	38.3	49.0		Total	27513	100.0
Suzhou	20.8	37.4	54.9				
Huzhou	20.0	35.9	55.0				

List of Figures

Figure 1 Location of Taihu Lake Basin and its administrative boundaries. (a) Yangtze River Delta, and (b) Taihu Lake Basin.

Figure 2 Decision tree classifier for identifying land use pattern in the Taihu Lake Basin

Figure 3 The method to simulate future coverage indices with an example of NDVI

Figure 4 Land use and land cover change in the Taihu Lake Basin during 1996 to 2016. (a) 1996 land pattern, (b) 2004 land pattern, and (c) 2016 land pattern.

Figure 5 Land coverage demonstrated by NDBI, NDVI and NDWI for 2016 in the Taihu Lake Basin. (a) 2016 NDBI, (b) 2016 NDVI, and (c) 2016 NDWI.

Figure 6 Spatial patterns of LST in the Taihu Lake Basin from 1996 to 2016. (a) 1996 LST, (b) 2004 LST, and (c) 2016 LST.

Figure 7 The simulated land use pattern and land coverage indices for the year 2026. (a) Projected land use pattern of 2026, (b) Land use change between 2016-2026, (c) 2026 NDBI, (d) 2026 NDVI, and (e) 2026 NDWI.

Figure 8 The projected LST for 2026 and its change between 2016–2026 in the Taihu Lake Basin. (a) Projected LST for the year 2026, and (b) Difference map of LST between 2016-2026.

Highlights

- We derived the spatiotemporal LST patterns in the Taihu Lake Basin from 1996 to 2026;
- A CA-Markov model was applied to project the 2026 land use pattern;
- We simulated the NDBI, NDVI and NDWI indices for 2026 and projected the 2026 LST pattern;
- LST has been increasing and the warming areas have been expanding since 1996;
- Mean LST increased by 2°C per decade in Su-Xi-Chang urban agglomeration between 1996 and 2026.

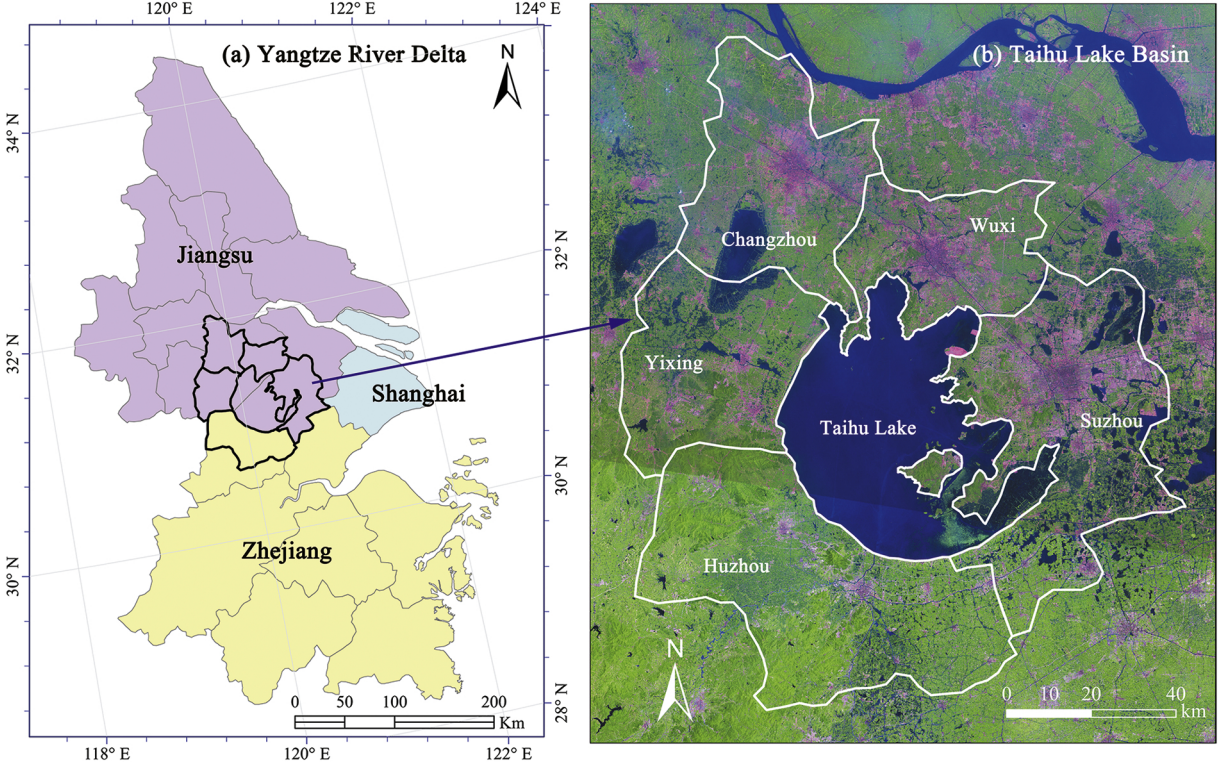
(a) Yangtze River Delta
N
120° E
122° E
124° E
34° N
32° N
30° N
28° N
118° E
Jiangsu
Shanghai
Zhejiang
0 50 100 200
Km
(b) Taihu Lake Basin
Changzhou
Wuxi
Yixing
Taihu Lake
Suzhou
Huzhou
0 10 20 40
km

Figure 1

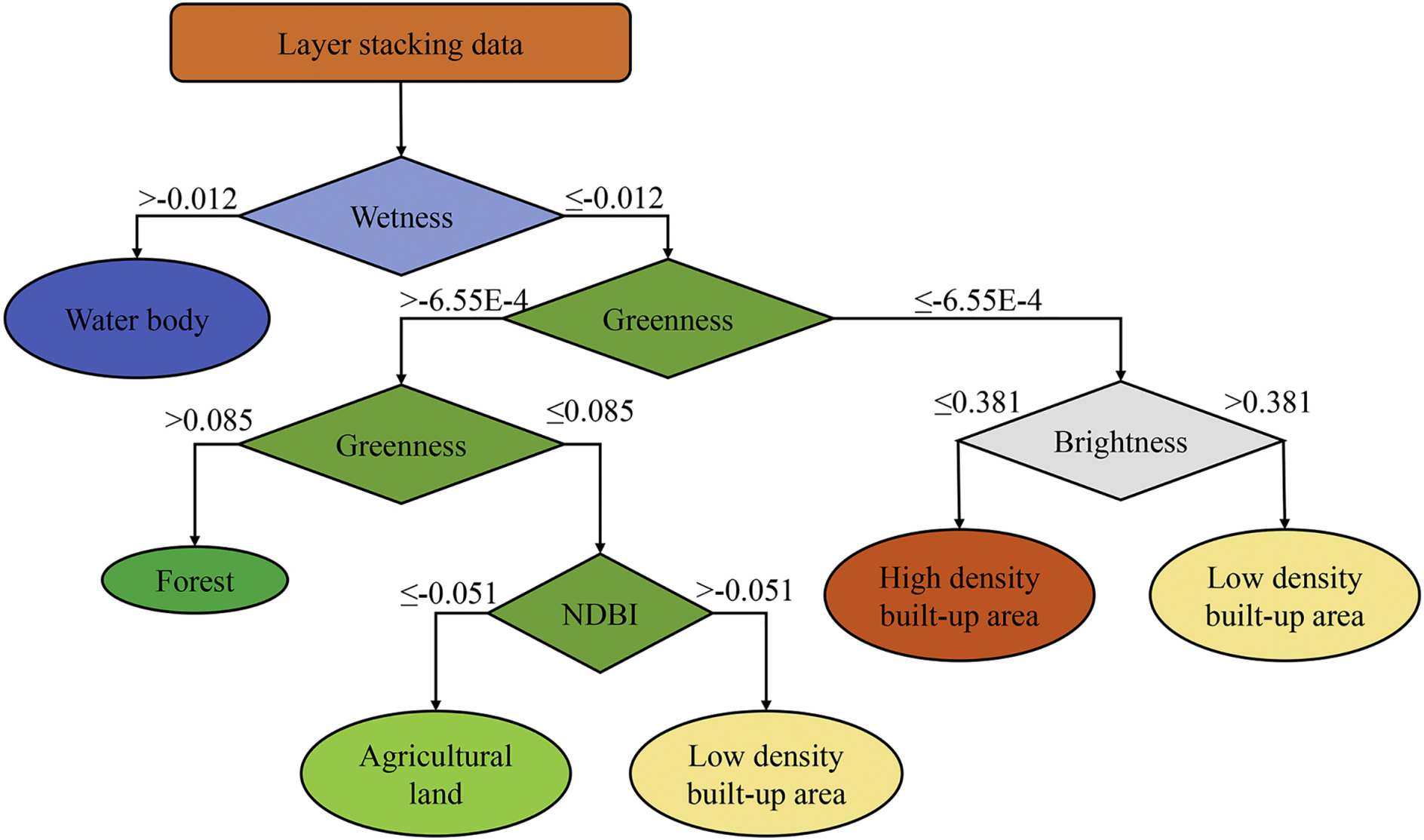
Layer stacking data
Wetness
>-0.012
≤-0.012
Water body
Greenness
>-6.55E-4
≤-6.55E-4
Greenness
>0.085
≤0.085
Brightness
≤0.381
>0.381
Forest
NDBI
≤-0.051
>-0.051
High density built-up area
Low density built-up area
Agricultural land
Low density built-up area

Figure 2

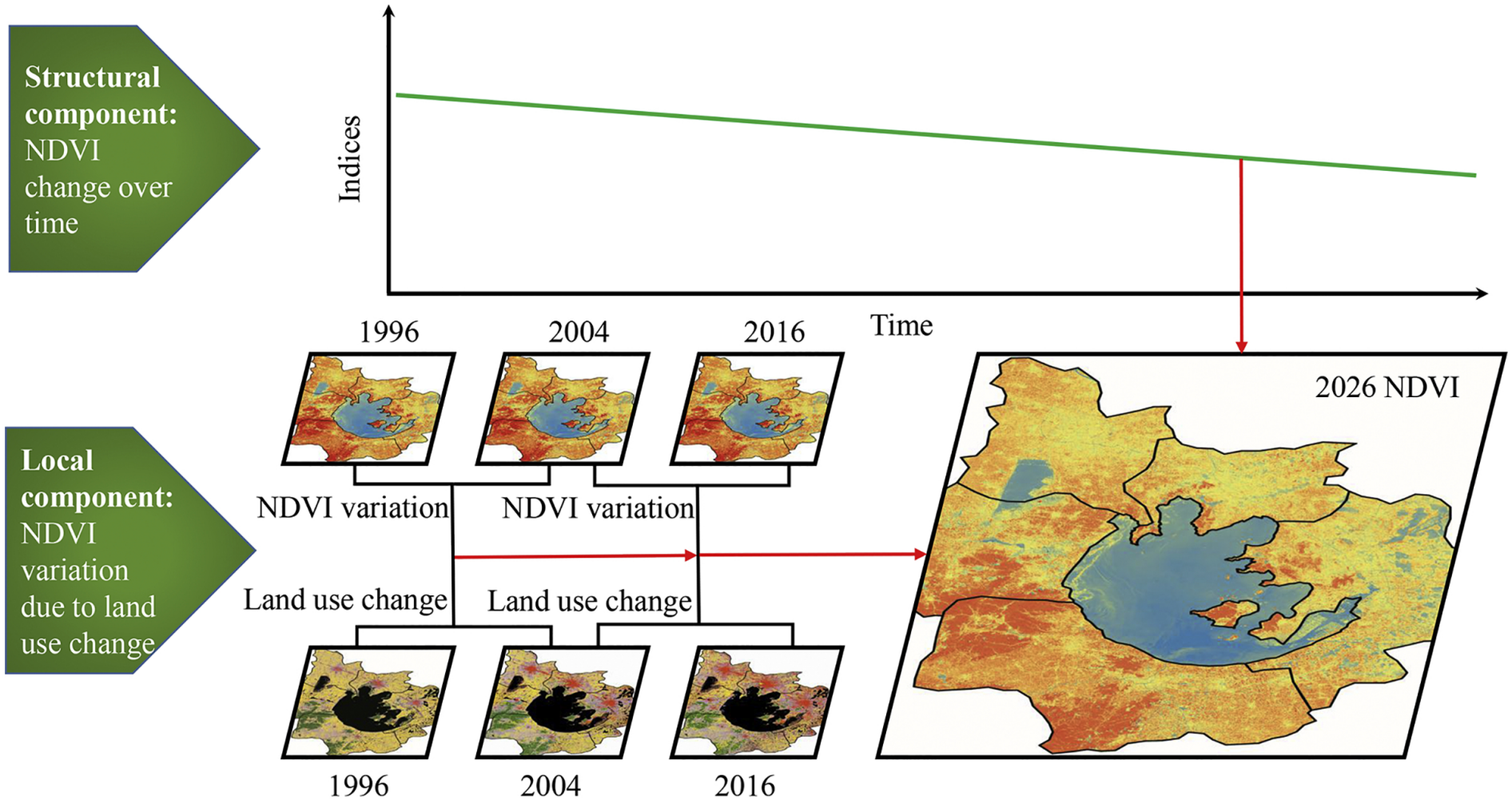
Structural component: NDVI change over time
Indices
Time
1996
2004
2016
2026 NDVI
Local component: NDVI variation due to land use change
NDVI variation
NDVI variation
Land use change
Land use change
1996
2004
2016

Figure 3

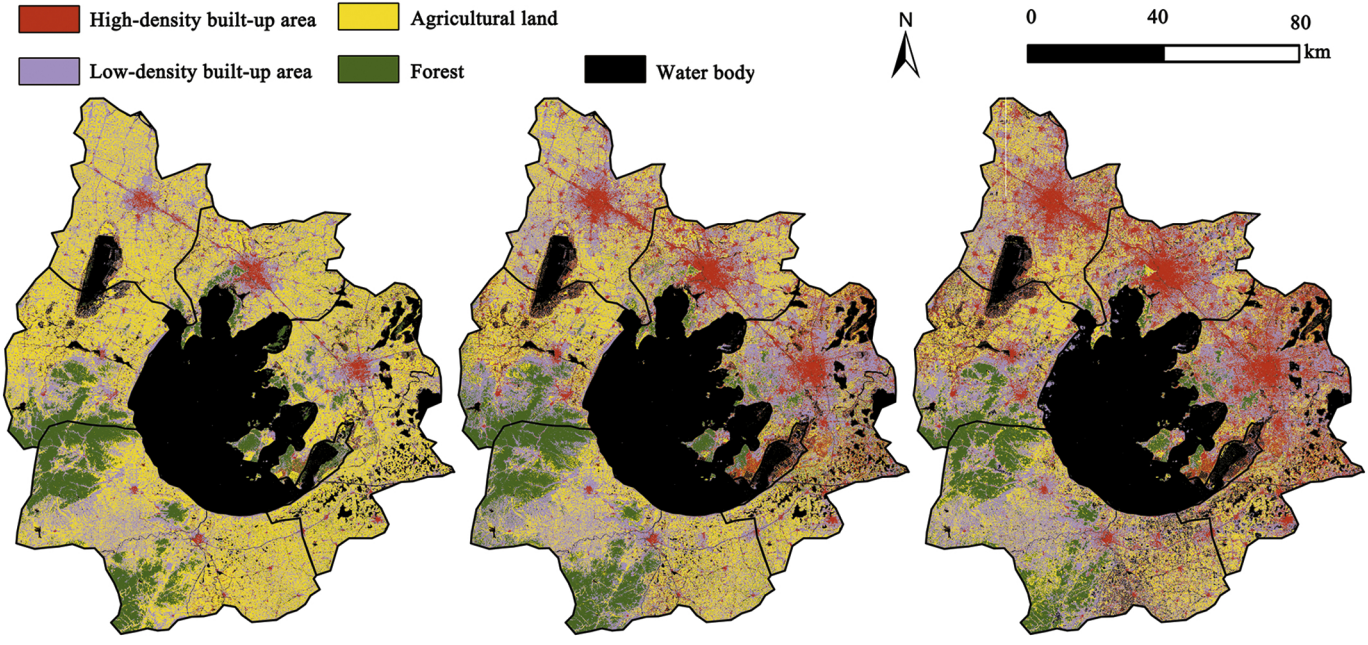
High-density built-up area
Agricultural land
Low-density built-up area
Forest
Water body
N
0
40
80
km
(a) 1996 land use pattern
(b) 2004 land use pattern
(c) 2016 land use pattern

Figure 4

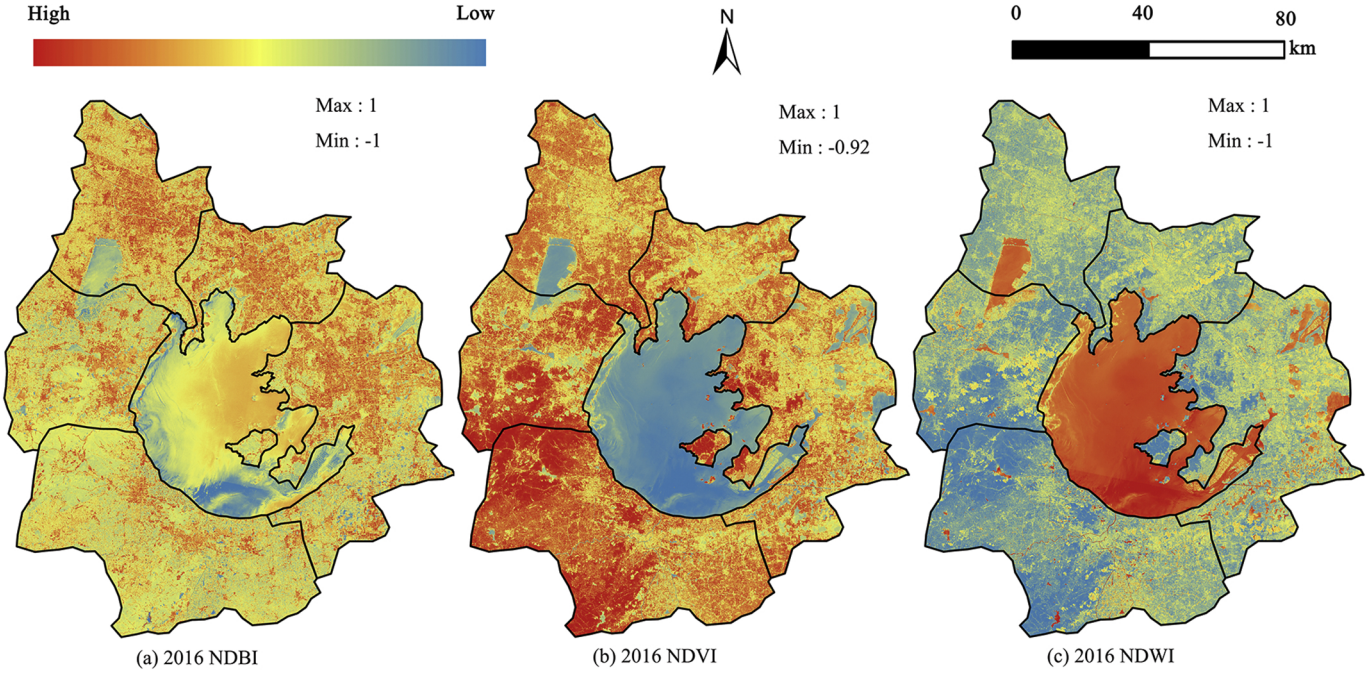
High
Low
N
0
40
80
km
Max : 1
Min : -1
(a) 2016 NDBI
Max : 1
Min : -0.92
(b) 2016 NDVI
Max : 1
Min : -1
(c) 2016 NDWI

Figure 5

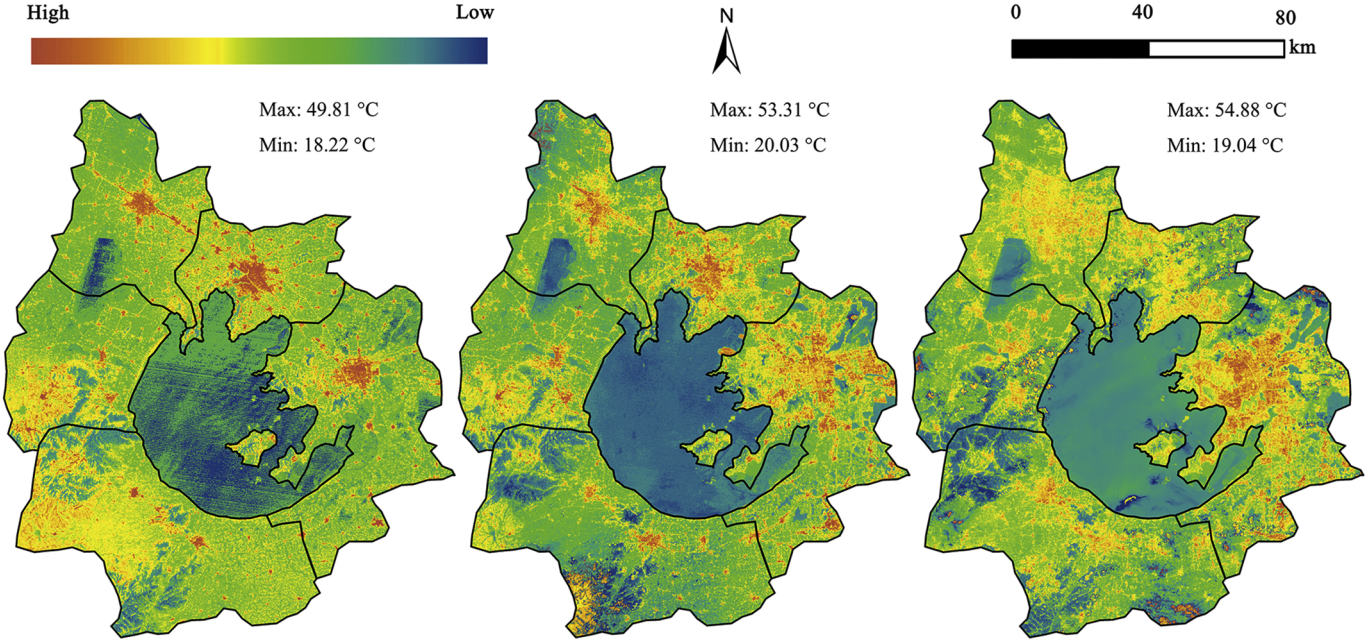
High
Low
N
0
40
80
km
Max: 49.81 °C
Min: 18.22 °C
Max: 53.31 °C
Min: 20.03 °C
Max: 54.88 °C
Min: 19.04 °C
(a) 1996 LST
(b) 2004 LST
(c) 2016 LST

Figure 6

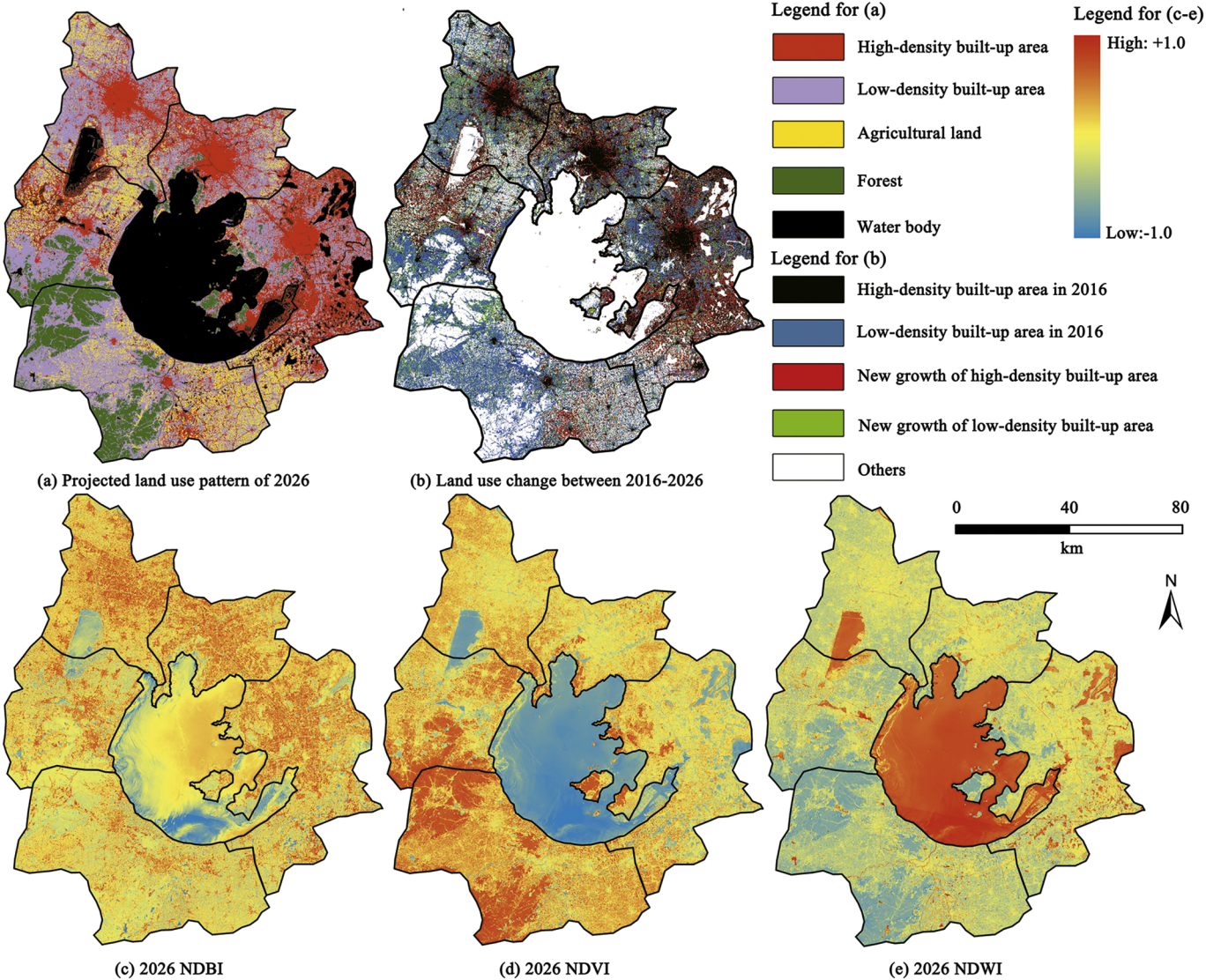
Legend for (a)
High-density built-up area
Low-density built-up area
Agricultural land
Forest
Water body
Legend for (c-e)
High: +1.0
Low:-1.0
Legend for (b)
High-density built-up area in 2016
Low-density built-up area in 2016
New growth of high-density built-up area
New growth of low-density built-up area
Others
0
40
80
km
N
(a) Projected land use pattern of 2026
(b) Land use change between 2016-2026
(c) 2026 NDBI
(d) 2026 NDVI
(e) 2026 NDWI

Figure 7

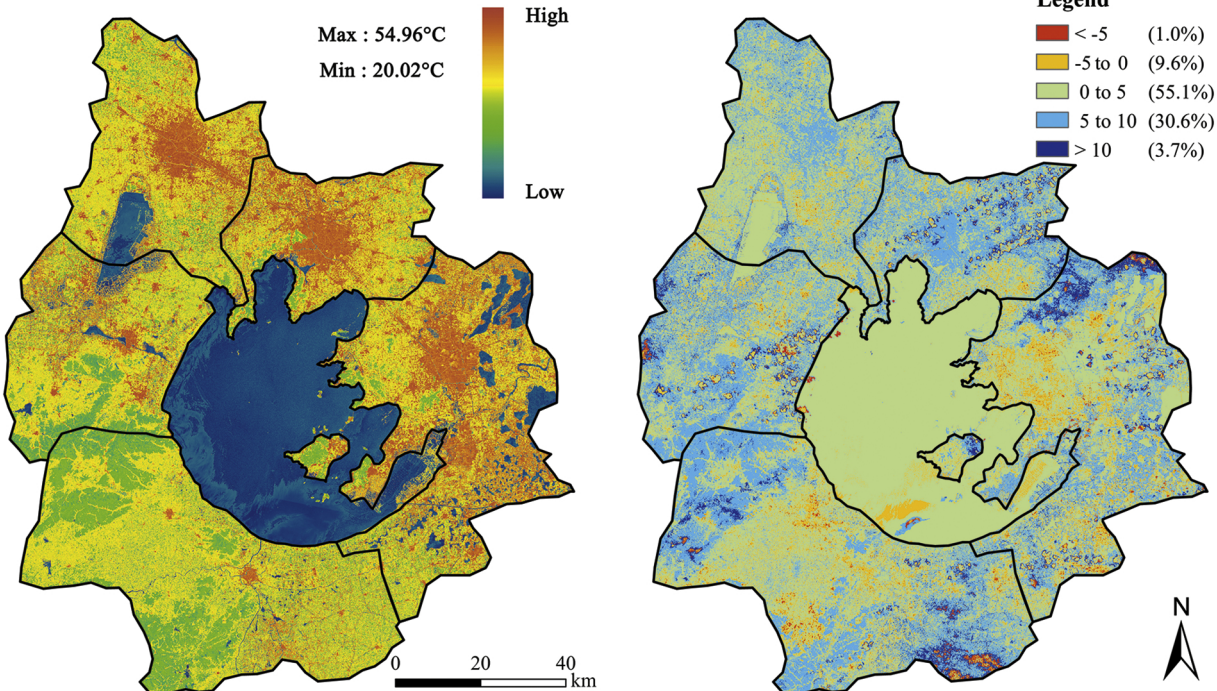

(a) Projected LST for the year 2026

(b) Difference map of LST between 2016-2026

Figure 8